Effect of Particle-Induced Voids on Evanescent Coupling in Silicon Photonics Heterogeneous Integration

Yang Liu, Jing Zhang, Evangelia Delli, and Gunther Roelkens, *Senior Member, IEEE*

***Abstract*—Supporting increasingly complex on-chip functionalities necessitates efficient heterogeneous integration of active components (e.g., InP lasers, $LiNbO_3$ modulators) in silicon photonics. However, deep-submicrometer particles and the resulting voids at the bonding interface of the integrated components can severely degrade evanescent coupling efficiency. In this paper, we combine an elastomechanical model and coupled-mode theory to quantify void-induced loss in two representative architectures: InP-on-Si lasers and $LiNbO_3$-on-Si_3N_4 modulators. For lasers, the impact is strongly location dependent: a 100 nm particle in a taper region incurs a 0.913 dB coupling loss versus 0.058 dB mid-device ($> 15\times$ increase). Increasing the separate confinement heterostructure (SCH) thickness from 25/25 nm to 100/100 nm suppresses higher-order mode excitation and flattens the loss response. Optoelectronic modeling confirms that this optical robustness far outweighs the marginal penalty in carrier injection efficiency. For modulators, replacing a slab $LiNbO_3$ film with a rib waveguide and employing a compact adiabatic Si_3N_4/$LiNbO_3$ taper confines the mode away from the electrodes and maintains low void-induced loss for particles up to sub-micrometer sizes. These results underscore the need for robust interfaces achieved through coordinated optimization of the layer stack, coupling scheme, and device geometry. Based on these insights, we propose design guidelines for void-tolerant evanescent interfaces on the silicon photonics platform, enabling higher yield in densely integrated heterogeneous photonic systems.**

***Index Terms*—Silicon photonics, heterogeneous integration, evanescent coupling, semiconductor lasers, modulators.**

I. Introduction

Silicon photonics (SiPh) is the dominant platform for photonic integrated circuits, enabled by its mature fabrication process flows and scalability [1], [2], [3], [4]. To overcome silicon's inherent limitations in active photonic functionalities, notably its inefficient light emission and weak electro-optic effects, heterogeneous integration techniques are essential to extend the platform's reach. Techniques such as micro-transfer printing (μTP) and wafer bonding [5], [6], [7], [8] enable the integration of critical non-CMOS-compatible devices: III-V semiconductors provide efficient on-chip light sources, while materials like thin-film lithium niobate ($LiNbO_3$) enable high-speed, low-loss electro-optic modulators for data transmission [9], [10], [11], [12], [13]. This heterogeneous integration is fundamental to achieving fully integrated photonic systems on chip.

Received 13 May 2026; revised 17 July 2026; accepted 21 July 2026. Date of publication 28 July 2026; date of current version 10 August 2026. This work was supported in part by the PhotonixFAB project under Grant 101111896 and in part by the Dutch Growth Fund PhotonDelta project. *(Corresponding author: Yang Liu.)*

The authors are with the Photonics Research Group, INTEC, Ghent University - imec, 9052 Ghent, Belgium (e-mail: yangyliu.liu@ugent.be).

Digital Object Identifier 10.1109/JPHOT.2026.3717815

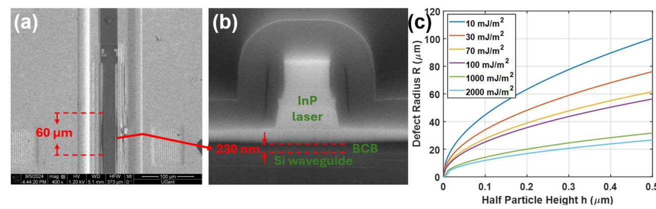

Fig. 1. (a) SEM image of a particle-induced void in an InP-on-Si laser fabricated by μTP and (b) an FIB cross-section cut through the center of the particle site. (c) Relationship between half the particle height and the resulting defect radius.

However, backend fabrication processes inherently introduce interfacial contaminants during bonding. While front-end CMOS processes are carried out in advanced cleanrooms, back-end heterogeneous integration inevitably introduces deep-submicrometer particle contamination. Completely eliminating these particles simply by increasing cleanroom standards is practically unfeasible and cost-prohibitive. Consequently, localized voids induced by particles with typical dimensions ranging from 100 nm to 500 nm are considered as intrinsic statistical limitations of current bonding and μTP workflows. Furthermore, given the large footprint of adiabatic tapers (often several tens of micrometers long) required for efficient mode transitions in densely integrated silicon photonics, the statistical probability of a particle landing within the critical phase-matching region is significant. These defects disrupt evanescent field coupling, which is the primary method for coupling light between the silicon circuit and the heterogeneous devices. Consequently, substantial optical power loss occurs, which is particularly crippling for integrated lasers and modulators.

In this work, we present a comprehensive quantitative investigation of particle-induced degradation in evanescent coupling efficiency across heterogeneous photonic platforms. Our study encompasses two key integration scenarios: (1) coupling between InP optical amplifier active regions and silicon waveguides (WGs), and (2) coupling between thin-film $LiNbO_3$ modulators and Si_3N_4 WGs. We assess the location dependence of void-induced coupling loss and analyze how particle-induced deformation at the bonding interface leads to

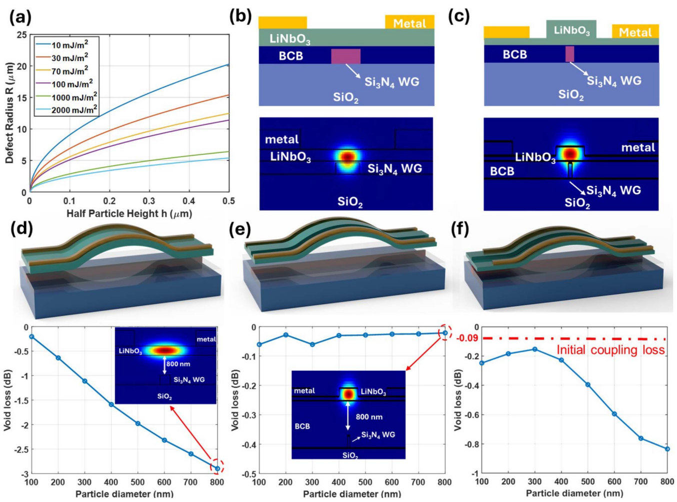

Fig. 2. Particle-induced voids in $LiNbO_3$-on-Si_3N_4 modulators. (a) Defect radius as a function of half the particle height for different bonding energies. (b) Cross-section and fundamental-mode profile of the slab $LiNbO_3$-on-Si_3N_4 structure. (c) Cross-section and fundamental-mode profile of the rib $LiNbO_3$-on-Si_3N_4 structure. (d) Void-induced loss versus particle diameter for the slab structure. (e) Corresponding loss for the rib-waveguide structure. (f) Void-induced loss versus particle diameter when the particle is located at the center of the rib taper; the dashed line indicates the defect-free coupling loss. The interfacial material is modeled as BCB.

integrated component bending, thereby degrading evanescent coupling. Crucially, we evaluate the resilience of III–V epitaxial layer designs to such deformation-induced coupling loss. By tailoring epitaxial layer structures, we demonstrate enhanced tolerance to bonding-related perturbations. We also demonstrate the benefits of using patterned $LiNbO_3$ waveguides compared to $LiNbO_3$ slab-based hybrid modulators. These insights offer actionable design principles for robust evanescent coupling in heterogeneous photonic devices, paving the way for scalable and reliable photonic systems-on-chip.

II. Particle-Induced Deformation of Heterogeneous Devices on SiPh

To pinpoint the mechanical origin of the observed coupling losses, we employ an elastomechanical model to analyze the impact of interfacial contamination. Deformation induced by particles at the interface is quantitatively evaluated through elastomechanical analysis. In this framework, the overall deformation depends on the particle size and the bonding strength after wafer bonding or μTP. For the heterogeneous bonding process, the defect introduced by a particle of height $2h$ has been described in [14].

The defect radius R is given by

$$R = \left[\frac{1.3\, E_1\, t_1^3\, E_2\, t_2^3}{\gamma \left(E_1\, t_1^3 + E_2\, t_2^3 \right)} \right]^{\frac{1}{4}} h^{\frac{1}{2}} \tag{1}$$

where E_i is the biaxial Young's modulus and t_i the thickness of wafer i, while γ represents the bonding energy. This expression applies to relatively large defects. When the computed R becomes too small, an elastomechanical instability arises, and the defect radius is better described by

$$R = \frac{h^2\,(E_1 + E_2)}{6\gamma} \tag{2}$$

In μTP, a thin functional layer, typically a few micrometers thick, is bonded to a substrate that is hundreds of micrometers thick, resulting in a strongly asymmetric mechanical structure. By combining Equations (1) and (2), Fig. 1(c) maps the transition between these regimes across particle sizes and bonding energies γ. For a typical μTP process with $\gamma \approx 70\,\mathrm{mJ/m^2}$, our scanning electron microscopy (SEM) and focused ion beam (FIB) characterizations provide direct experimental validation for this elastomechanical model. As shown in Fig. 1(a) and the precise center-cut FIB cross-section in Fig. 1(b), a trapped BCB residue particle with a measured total height of 230 nm ($2h = 230\,\mathrm{nm}$) creates an unbonded void region. According to our calculation in Fig. 1(c), this specific particle height corresponds to a theoretical defect radius of approximately $55.2\,\mu\mathrm{m}$, which is consistent with the observed lateral extent of the void.

Although introduced here for μTP, Eqs. (1) and (2) are based on elastic bending and interfacial adhesion and are not limited to a specific bonding process. Their application to other bonding structures requires the corresponding layer thicknesses, elastic moduli, and bonding energy. The present model assumes a single isolated defect and uniform interfacial adhesion. Large or irregular particle clusters may produce more complex deformation

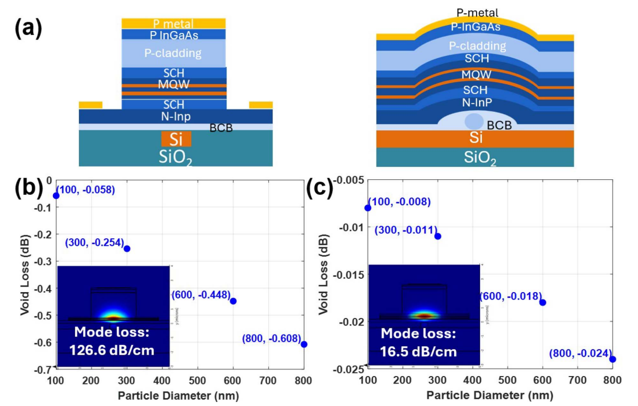

Fig. 3. (a) Schematic cross sections of the InP-on-Si laser perpendicular (left) and parallel (right) to the propagation direction; Void loss vs. particle diameter at the InP-on-Si laser midpoint for SCH = (b) 25/25 nm and (c) 100/100 nm. Insets: corresponding defect-free mode profiles and midpoint modal losses.

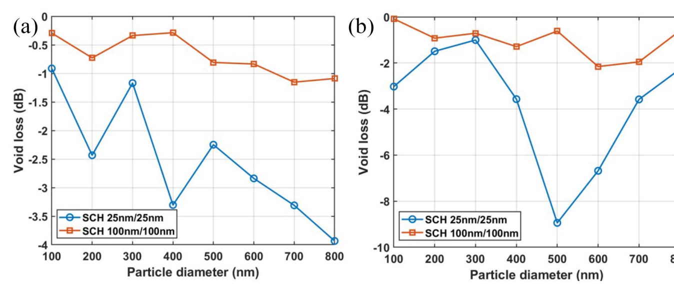

Fig. 4. Void loss (dB) versus particle diameter for the full-coupling (a) and partial-coupling (b) with the SCH layer thicknesses of 25/25 and 100/100 nm.

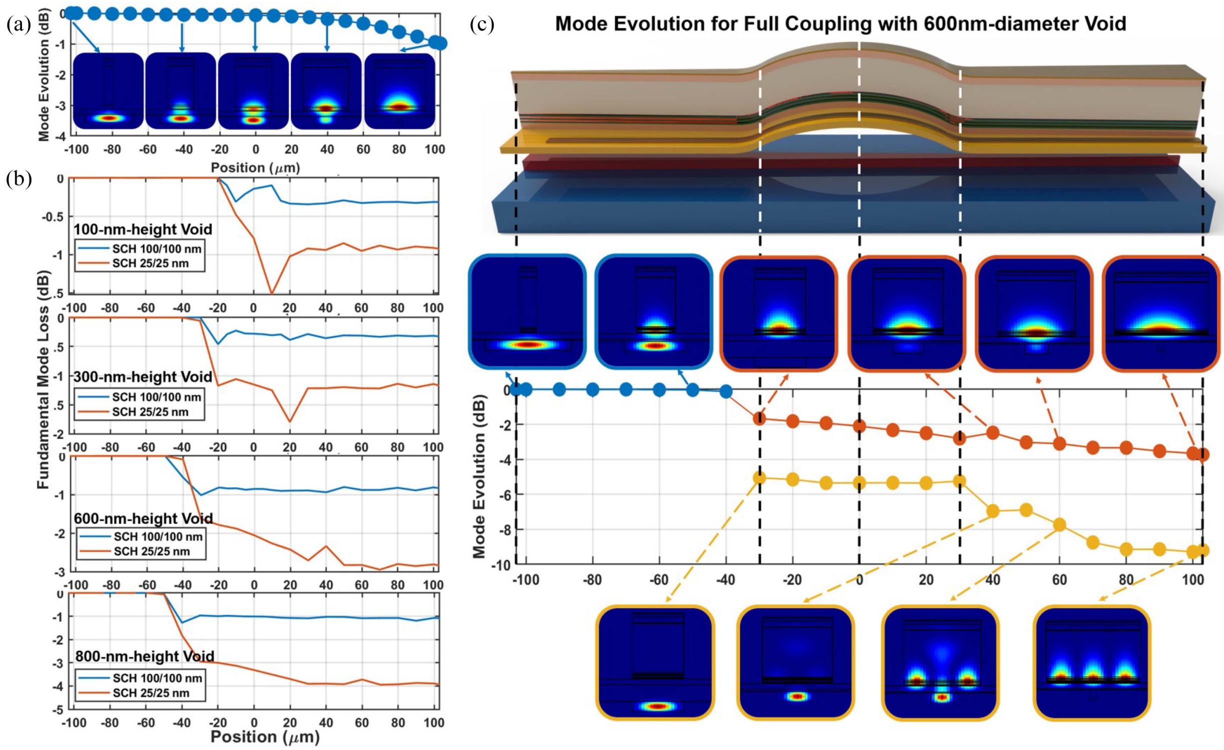

Fig. 5. Mode evolution along the full-coupling taper (tip-to-end): (a) defect-free adiabatic taper reference; (b) optical mode evolution for various particle diameters with SCH layers of 25/25 nm and 100/100 nm; (c) zoomed-in analysis of the mode splitting for 25/25 nm SCH with a 600-nm-diameter void case (The yellow dotted line indicates the fraction of the input power coupled to the dominant higher-order mode. The field profile of the corresponding higher-order mode is shown in the insets).

profiles and are beyond the scope of this study. The quantitative results reported here are specific to DVS-BCB adhesive bonding.

III. Void in $LiNbO_3$-on-Si_3N_4 Modulators

Heterogeneous integration of lithium niobate, with its strong Pockels effect [15], [16], [17], [18], onto silicon nitride waveguides offers a promising solution to overcome the lack of high-speed modulation capability in Si_3N_4 and to some extent Si platforms [19], [20], [21]. We consider a typical $LiNbO_3$-on-Si_3N_4 hybrid modulator comprising a 300-nm-thick X-cut $LiNbO_3$ film bonded through a thin DVS-BCB layer to a 1-μm-wide, 300-nm-thick Si_3N_4 waveguide. While adhesive-free direct bonding is feasible on sufficiently smooth surfaces [22], it imposes stringent roughness and topography requirements that are difficult to meet on processed photonic wafers; DVS-BCB adhesive bonding tolerates such non-idealities while providing strong adhesion and thermal stability, and is therefore adopted here. Light propagating through the Si_3N_4 waveguide is phase-modulated by the Pockels effect in the overlying $LiNbO_3$. The applied electric field alters the refractive index of the $LiNbO_3$ layer, shifting the effective index seen by the guided mode. In practice, this bonded structure acts as a highly efficient phase modulator. The integration faces critical yield challenges from interfacial particles at the phase-shifter level. A void in the active modulation region will cause localized optical loss and phase errors, inherently degrading the standalone modulation performance and disrupting signal integrity.

According to (1) and (2) with the mechanical parameters of $LiNbO_3$[23], Fig. 2(a) shows the dependence of the defect radius on half the particle height for $LiNbO_3$/Si_3N_4 bonding ($\gamma \approx 70\,\mathrm{mJ/m^2}$ for the general μTP process).

In our finite-element simulations, which are performed at 1550 nm, we treat each interfacial contaminant as a particle with the same refractive index as the surrounding BCB layer. In defect-free regions (Fig. 2(b)), the hybrid mode exhibits dual confinement: 50.8% resides in the top $LiNbO_3$ layer (40-nm-thick DVS-BCB bonding layer), while the remaining optical power resides in the 1- μm-wide Si_3N_4 waveguide.

As we sweep the particle diameter from 100 nm upward, the guided mode shifts toward the $LiNbO_3$ layer and its fractional confinement in the top $LiNbO_3$ film rises accordingly. As shown in the extreme event of an 800 nm-diameter inclusion (Fig. 2(d)), the mode shifts upward in the $LiNbO_3$. Because $LiNbO_3$ confines light less tightly than Si_3N_4, the mode overlaps the metal electrodes on top of the $LiNbO_3$, where the absorption in the electrodes further reduces transmitted power. Consequently, as the particle diameter increases from 100 nm to 800 nm, the void-induced loss increases from 0.21 dB to 2.90 dB as shown in Fig. 2(d).

To mitigate this void sensitivity, we adopt a full power-transfer architecture based on a $LiNbO_3$ rib waveguide instead of the slab $LiNbO_3$ film. The rib geometry (width 1.5 μm, thickness 200 nm) confines the optical mode within the $LiNbO_3$ ridge, while the Si_3N_4 waveguide width is reduced to 200nm, as shown in Fig. 2(c). Optical power is fully transferred from

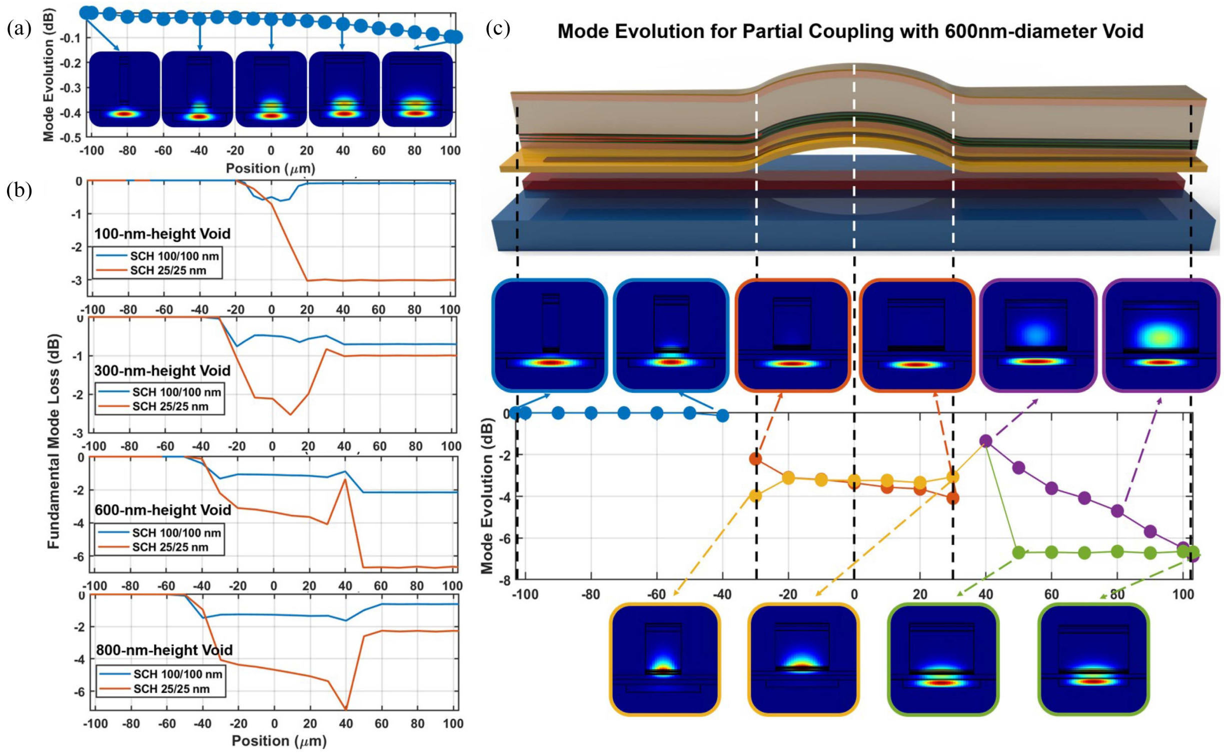

Fig. 6. Mode evolution along the partial-coupling taper (tip-to-end): (a) defect-free adiabatic taper reference; (b) optical mode evolution for various particle diameters with SCH layers of 25/25 nm and 100/100 nm; (c) zoomed-in analysis of the mode splitting for 25/25 nm SCH with a 600-nm-diameter void case (the differently colored dotted lines indicate the fraction of the input power coupled to particular modes. The field profile of the corresponding modes is shown in the insets).

the Si_3N_4 guide to the $LiNbO_3$ rib via a compact adiabatic taper: the Si_3N_4 core narrows from $1.5\,\mu m$ to 200 nm while the $LiNbO_3$ rib simultaneously expands from 200 nm to $1.5\,\mu m$ over a $40\,\mu m$-long taper. The defect-free coupling loss is 0.09 dB. This final rib waveguide confines the mode to the rib ridge, minimizes electrode overlap, and reduces the propagation loss to $5.6 \times 10^{-3}\,dB/cm$. With a void present, the mode remains rib-confined and incurs negligible additional loss even for particle diameters up to 800 nm as shown in Fig. 2(e), because the induced curvature corresponds to large bend radii ($\sim$ 60–80 μm) for which bend loss is negligible in a well-designed rib waveguide.

For robustness, we also examine defects within the taper. Placing a void at the midpoint of the taper breaks strict adiabaticity and increases the void-induced insertion loss from 0.20 dB to 0.83 dB for particle diameters ranging from 100 nm to 800 nm, compared to a 0.09 dB coupling loss for a void-free interface (Fig. 2(f)). Nevertheless, this remains well below the loss observed for the hybrid mode configuration. The findings highlight rigorous particle control for slab $LiNbO_3$ modulators made by adhesive micro-transfer printing and point to rib-waveguide full power transfer as a void-tolerant solution for $LiNbO_3$-on-Si_3N_4.

IV. Void in InP-on-Si Lasers

A. Void in Middle Section of InP-on-Si Lasers

Heterogeneous integration of III-V materials, such as InP and GaAs, onto silicon waveguides enables the incorporation of efficient light sources and optical amplifiers, addressing one of the fundamental limitations of silicon photonics [24], [25], [26], [27], [28]. The integration of InP multi-quantum-well (MQW) lasers on silicon photonics faces critical power degradation due to particle-induced deformation at bonding interfaces. Our analysis reveals a strong dependence of this sensitivity on epitaxial layer design. For InP-on-Si evanescent-coupled lasers, the epitaxial stack typically includes an n-InP contact layer; InAlGaAs quantum wells and barriers; lower and upper separate confinement heterostructure (SCH) layers; a p-InP cladding; and a p-InGaAs cap/contact layer [29], [30], as shown in Fig. 3(a). Among them, the SCH layers are especially critical, as they confine both the optical field and injected carriers into the MQW region, boosting optical gain and driving down laser threshold currents.

For a standard InP laser structure with 25-nm-thick SCH layers, the finite-difference time-domain (FDTD) simulations (Fig. 3) demonstrate void loss escalation from 0.06 dB to 0.61 dB as particle diameter increases from 100 nm to 800 nm, when the particle is located in the middle of the printed III-V coupon. The localized deformation redistributes the optical mode, increasing field overlap with lossy upper layers (p-InP, p-InGaAs, p-metal, etc.).

By increasing the SCH layer thickness to 100 nm, the MQW confinement factor, Γ_{MQW}, improves from 16.3% to 20.2%, reducing the optical field's overlap with the lossy upper layers. As a result, the void loss for 800-nm particles is dramatically reduced from 0.61 dB to 0.03 dB. These results underscore that SCH layer engineering is a critical strategy for achieving deformation-insensitive bonded lasers, maintaining void-induced losses below 0.1 dB for high-yield silicon photonics heterogeneous integration.

B. Void in Taper Section of InP-on-Si Lasers

Our analysis also finds a strong dependence of void-induced loss sensitivity on void location. For an integrated evanescent-coupling laser on chip, a well-designed adiabatic taper plays a critical role in enabling high-quality evanescent coupling in silicon photonics. In our optimized adiabatic taper, the InP layer's width at the top gradually expands from 0.5 μm to 3.2 μm [31], [32]. To transfer light from the silicon underlayer into this widening ridge, we employ two coupling schemes. In the full-coupling approach, the silicon taper's width continuously decreases from 3 μm down to about 0.2 μm; as it narrows, the mode is gradually transferred entirely into the III-V-ridge by the taper's end. Alternatively, in the partial-coupling scheme, the silicon stays 3 μm wide throughout and instead of a complete power transfer, the optical field evolves into a hybrid mode that occupies both the silicon WG and the InP active region. This design can mitigate the saturation effect of the amplifier.

In the worst case, an interfacial particle lies within the phase-matching section of the taper. We model power evolution with a two-supermode coupled-mode framework cast in a transfer-matrix form along the taper direction z [33]. The complex modal amplitudes $X_1(z)$ and $X_2(z)$ obey:

$$\frac{d}{dz}\begin{bmatrix} X_1(z) \\ X_2(z) \end{bmatrix} = -i \begin{bmatrix} \beta_1 & \kappa \\ \kappa & \beta_2 \end{bmatrix} \begin{bmatrix} X_1(z) \\ X_2(z) \end{bmatrix} \tag{3}$$

where $\beta_{1,2}$ are the local propagation constants of the two supermodes (the detuning is $\Delta\beta = \beta_1 - \beta_2$) and κ is their coupling coefficient. Within the void section, we approximate the perturbation as a local coupler of effective length $L_{\text{eff}}(d)$. Solving (3) over this section gives the transferred power as a function of the particle diameter d:

$$P_{\text{transfer}}(d) \approx \underbrace{\frac{\kappa(d)^2}{\kappa(d)^2 + \left(\frac{\Delta\beta(d)}{2}\right)^2}}_{\text{decaying envelope}} \underbrace{\sin^2\left(\sqrt{\kappa(d)^2 + \left(\frac{\Delta\beta(d)}{2}\right)^2}\, L_{\text{eff}}(d)\right)}_{\text{beating term}} \tag{4}$$

As the void diameter increases, the enlarged gap reduces the modal overlap, thereby lowering the coupling coefficient $\kappa(d)$ and simultaneously increases the detuning $|\Delta\beta(d)|$ by shifting the local effective indices. Consequently, the prefactor in Eq. (4) decreases monotonically with d, which shows an overall downward trend. The $\sin^2(*)$ term produces the oscillations: a smaller particle can yield a larger loss when $L_{\text{eff}}(d)$ happens to be close to the half-beat length:

$$L_{\pi/2}(d) = \frac{\pi}{2\sqrt{\kappa(d)^2 + \left(\frac{\Delta\beta(d)}{2}\right)^2}} \tag{5}$$

The simulated void-induced loss versus particle diameter in Fig. 4 agrees with the theoretical analysis: it decreases with particle diameter while exhibiting damped oscillations for both the fully-coupled and the partial-coupling tapers. The ripple amplitude differs due to their distinct $\kappa(z)$ and $\Delta\beta(z)$ profiles.

Fig. 5 shows how an interfacial void placed in the phase-matching section alters the adiabatic transfer from the Si-guided mode to the III-V fundamental mode. The defect-free reference (Fig. 5(a)) shows near-ideal behavior: power follows the adiabatic path through the phase-matching section and exits in the top III-V fundamental mode with a total insertion loss of 0.98 dB including material absorption (pure coupling loss < 0.04 dB). When a 100-nm particle is introduced in the phase-matching section for a standard structure with 25/25 nm SCH layers (Fig. 5(b)), the hybrid supermode splits: 84.0% of the power is drawn into the MQW region while 15.9% remains in the Si waveguide, producing a local $\sim$1.5 dB dip that partially recovers downstream; the resulting void-induced loss is 0.91 dB. For larger particles the perturbation strengthens and the Si-dominant supermode (optical power is primarily confined in the silicon underlayer) fails to reconvert before the taper exit (e.g., 600 nm particle diameter in Fig. 5(c)), so a substantial fraction of power couples to lossy higher-order modes (HOMs) in the III-V section; only 47.0% remains in the fundamental mode at the output.

As shown in Fig. 5(b), increasing the SCH thickness from 25/25 nm to 100/100 nm markedly reduces void-induced loss. This improvement stems from two interconnected effects. First, the thicker SCH pulls the optical mode farther from the bonding interface, reducing its overlap with the void. This weakens the supermode coupling coefficient (κ) and increases the detuning ($|\Delta\beta|$), resulting in a very short effective interaction length (L_{eff}). The defect thus acts as a weak, detuned coupler that cannot meet the half-beat condition for significant power exchange, damping the oscillations. Second, the enhanced vertical confinement suppresses higher-order mode excitation, allowing any transient imbalance to efficiently reconvert to the fundamental mode before the taper exit. Consequently, the loss for the 100/100 nm design shows only shallow, flat dips, in stark contrast to the deep, oscillatory loss of the 25/25 nm case.

Fig. 6 illustrates the mode evolution in a partial-coupling taper. In the defect-free reference case (Fig. 6(a)), the Si-guided mode is adiabatically transformed into a hybrid mode shared by the Si waveguide and the III–V ridge. The introduction of an interfacial void disrupts this process. The void-induced loss versus particle diameter (Fig. 4(b)) exhibits pronounced oscillations, indicating strong mode mixing. The partial-coupling taper is more sensitive to these defects than a fully coupled design because a defect in the phase-matching region efficiently mixes the supermodes, and the remaining taper length is insufficient for recovery. This is exemplified by the 600-nm void case (Fig. 6(c)): within the defect, power shuttles between a Si-dominant and a III–V-dominant supermode. After

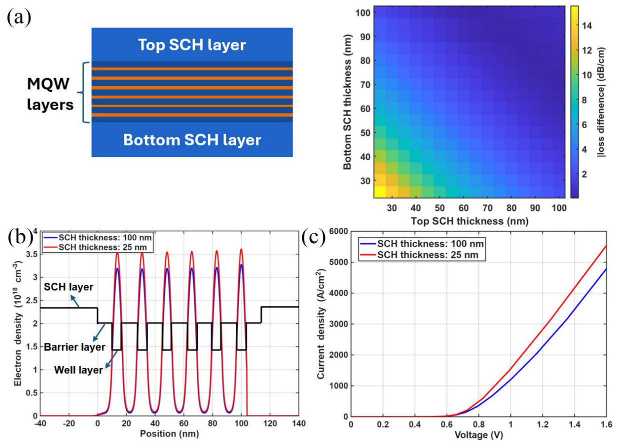

Fig. 7. (a) Heatmap of the absolute modal loss variation (|Δloss|) when the bonding BCB thickness fluctuates from 70 nm to 30 nm, mapped against varying top and bottom SCH thicknesses; (b) localized electron density across the multi-quantum wells; and (c) current density-voltage (J-V) characteristics between the 25/25 nm and 100/100 nm SCH designs.

the void, a brief partial recombination occurs, but continued strong coupling leads to further splitting. Consequently, only about 21.5% of the optical power is recovered in the fundamental hybrid mode at the output, with the remainder residing in the lossy higher-order content. Increasing the SCH thickness to 100/100 nm moves the field farther from the interface and reduces gap sensitivity; the effective interaction created by the void becomes shorter and weaker, the oscillations in Fig. 4(b) are strongly damped, and the overall void-induced loss for 100–800 nm particles is markedly lower than with the 25/25 nm stack. This behavior highlights the critical sensitivity of the taper's performance to defects near the phase-matching point.

C. Trade-Off Analysis: Optical Robustness Vs. Active Performance

While expanding the SCH layers effectively isolates the optical mode from bonding interface perturbations, modifying the epitaxial stack inherently alters the optoelectronic properties of the active region. We quantitatively evaluate the trade-off between the gained optical robustness and the active performance penalty using optoelectronic TCAD simulations (nextnano) [34].

The primary optical benefit of a thicker SCH is established in Fig. 7(a). To emulate the interface gap variations induced by deep-submicrometer particles, we swept the localized DVS-BCB bonding thickness from 70 nm down to 30 nm. For a standard 25/25 nm SCH design, this interfacial fluctuation produces a modal-loss variation (|Δloss|) exceeding 15 dB/cm, severely undermining device stability. In contrast, increasing the SCH thickness to 100/100 nm suppresses this variation to approximately 1 dB/cm, demonstrating that a thicker SCH yields a highly robust, deformation-insensitive optical mode.

To understand the underlying carrier injection dynamics, we examine the electron density distribution across the quantum wells at a standard injection level of around 5 kA/cm^2 (Fig. 7(b)). The 100/100 nm SCH design substantially increases the total volume of the undoped intrinsic region. This widened region prolongs the carrier transport time before they are captured by the quantum wells and increases non-radiative recombination within the SCH itself [35], [36], [37], [38]. Consequently, at the same current density, the steady-state electron density effectively confined within the multiple quantum wells is slightly lower for the 100 nm SCH design compared to the 25 nm design.

The widened intrinsic region also impacts the electrical transport. As illustrated in the J-V characteristics (Fig. 7(c)), the thicker SCH layers introduce a higher series resistance. Achieving the 5 kA/cm^2 current density requires a higher forward bias for the 100/100 nm structure (∼1.6 V) than for the 25/25 nm structure (∼1.5 V), indicating a slight penalty in power consumption.

In summary, the thicker SCH layer introduces a marginal electro-optical penalty, which is evidenced by the slightly reduced well carrier density and the increased operating voltage. However, from a system-level integration perspective, the massive enhancement in optical yield effectively eliminates void-induced radiation losses. This significant gain far outweighs the manageable degradation in active performance. These findings establish the adoption of thicker SCH layers as a highly practical design principle for resilient integrated photonic systems. During high-power operation, junction-temperature gradients may introduce additional thermal stress, while an interfacial void can also impede local heat dissipation toward the substrate. A fully coupled thermo-opto-mechanical analysis of these effects is beyond the scope of the present study and is left for future work.

V. Conclusion

Particle-induced voids at bonding interfaces can critically degrade device performance by disrupting phase matching and increasing radiation losses. Our study on evanescent coupled InP-on-Si lasers and $LiNbO_3$-on-Si_3N_4 modulators demonstrates that coupling sensitivity is strongly dependent on particle size, location, device geometry, and epitaxial layer design. Notably, particles situated in the phase-matching region induce complex mode splitting and increased radiation loss. For hybrid modulators, employing a rib-waveguide full-power transfer scheme effectively isolates the optical mode from void-induced bending and lossy electrodes. For integrated lasers, optimizing the epitaxial design by expanding the SCH layers dramatically enhances optical confinement and suppresses void-induced loss variations. Our optoelectronic trade-off analysis also confirms that the immense gain in optical robustness and yield far outweighs the marginal penalties in carrier injection efficiency and operating voltage. These findings underscore the necessity of coordinated multiphysics engineering, spanning layer stack optimization and coupling geometry, to achieve void-tolerant interfaces and high-yield silicon photonics heterogeneous integration. The broader principle of reducing optical sensitivity to bonding-interface deformation may also be applicable to emerging heterogeneous platforms, including BTO-on-Si modulators and quantum-dot lasers, although platform-specific optimization remains necessary.

REFERENCES

[1] S. Shekhar et al., "Roadmapping the next generation of silicon photonics," *Nature Commun.*, vol. 15, no. 1, 2024, Art. no. 751.

[2] D. Dai, D. Liang, and P. Cheben, "Next-generation silicon photonics: Introduction," *Photon. Res.*, vol. 10, no. 10, pp. NGSP1–NGSP3, 2022.

[3] S. Y. Siew et al., "Review of silicon photonics technology and platform development," *J. Lightw. Technol.*, vol. 39, no. 13, pp. 4374–4389, 2021.

[4] T. Komljenovic et al., "Heterogeneous silicon photonic integrated circuits," *J. Lightw. Technol.*, vol. 34, no. 1, pp. 20–35, 2016.

[5] G. Roelkens et al., "Present and future of micro-transfer printing for heterogeneous photonic integrated circuits," *APL Photon.*, vol. 9, no. 1, 2024.

[6] X. Zhang et al., "High-coherence parallelization in integrated photonics," *Nature Commun.*, vol. 15, no. 1, 2024, Art. no. 7892.

[7] Y. Liu, Z. Li, F. B. Atar, H. Muthuganesan, B. Corbett, and L. Wang, "Integration of high-performance InGaAs/GaN photodetectors by direct bonding via micro-transfer printing," *ACS Appl. Mater. Interfaces*, vol. 16, no. 8, pp. 10996–11002, 2024.

[8] Y. Liu et al., "Demonstration of n-Ga_2O_3/p-GaN diodes by wet-etching lift-off and transfer-print technique," *IEEE Electron Device Lett.*, vol. 42, no. 4, pp. 509–512, Aug. 2021.

[9] D. Liang et al., "High-performance quantum-dot distributed feedback laser on silicon for high-speed modulations," *Optica*, vol. 8, no. 5, pp. 591–593, 2021.

[10] T. Vanackere et al., "High-speed lithium niobate modulator on silicon nitride using micro-transfer printing," presented at CLEO: Sci. Innovations. San Jose CA, USA, May 7–12, 2023, paper STh1R, pp. 1.

[11] T. Vanackere et al., "Heterogeneous integration of a high-speed lithium niobate modulator on silicon nitride using micro-transfer printing," APL Photon., vol. 8, no. 8, 2023, Art. no. 086102.

[12] Y. Liu et al., "Widely tunable narrow-linewidth lasers with booster amplification on silicon photonics," *Opt. Exp.*, vol. 33, no. 10, pp. 22078–22086, 2025.

[13] D. Liang, X. Huang, G. Kurczveil, M. Fiorentino, and R. Beausoleil, "Integrated finely tunable microring laser on silicon," *Nature Photon.*, vol. 10, no. 11, pp. 719–722, 2016.

[14] Q.-Y. Tong and U. Goesele, "Semiconductor Wafer Bonding: Science and Technology," (Electrochemical society series). Hoboken, NJ, USA: Wiley Interscience, 1999.

[15] D. Chelladurai et al., "Barium titanate and lithium niobate permittivity and pockels coefficients from megahertz to sub-terahertz frequencies," *Nature Mater.*, vol. 24, no. 6, pp. 868–875, 2025.

[16] Y. Li, M. Sun, T. Miao, and J. Chen, "Towards high-performance pockels effect-based modulators: Review and projections," *Micromachines*, vol. 15, no. 7, 2024, Art. no. 865.

[17] Y. Hu et al., "Integrated electro-optics on thin-film lithium niobate," *Nature Rev. Phys.*, vol. 7, no. 5, pp. 237–254, 2025.

[18] J. Wang, S. Xu, J. Chen, and W. Zou, "A heterogeneous silicon on lithium niobate modulator for ultra-compact and high-performance photonic integrated circuits," *IEEE Photon. J.*, vol. 13, no. 1, Feb. 2021, Art. no. 4900112.

[19] M. Churaev et al., "A heterogeneously integrated lithium niobate-on-silicon nitride photonic platform," *Nature Commun.*, vol. 14, no. 1, 2023, Art. no. 3499.

[20] L. Chang et al., "Heterogeneous integration of lithium niobate and silicon nitride waveguides for wafer-scale photonic integrated circuits on silicon," *Opt. Lett.*, vol. 42, no. 4, pp. 803–806, 2017.

[21] L. Chen, Q. Xu, M. G. Wood, and R. M. Reano, "Hybrid silicon and lithium niobate electro-optical ring modulator," *Optica*, vol. 1, no. 2, pp. 112–118, 2014.

[22] Y. Liu et al., "A p-Si/n-GaN diode fabricated by nanomembrane lift-off and transfer-print technique," *Semicond. Sci. Technol.*, vol. 34, no. 10, 2019, Art. no. 105023.

[23] W. C. Jiang and Q. Lin, "Chip-scale cavity optomechanics in lithium niobate," *Sci. Rep.*, vol. 6, no. 1, 2016, Art. no. 36920.

[24] M. Tang et al., "Integration of III-V lasers on Si for Si photonics," *Prog. Quantum Electron.*, vol. 66, pp. 1–18, 2019.

[25] Z. Wang, R. Yao, S. F. Preble, C.-S. Lee, L. F. Lester, and W. Guo, "High performance InAs quantum dot lasers on silicon substrates by low temperature Pd-GaAs wafer bonding," *Appl. Phys. Lett.*, vol. 107, no. 26, 2015, Art. no. 261107.

[26] G. Roelkens, D. V. Thourhout, R. Baets, R. Nötzel, and M. Smit, "Laser emission and photodetection in an inp/ingaasp layer integrated on and coupled to a silicon-on-insulator waveguide circuit," *Opt. Exp.*, vol. 14, no. 18, pp. 8154–8159, 2006.

[27] S.-S. Sui, M.-Y. Tang, Y.-D. Yang, J.-L. Xiao, Y. Du, and Y.-Z. Huang, "Mode investigation for hybrid microring lasers with sloped sidewalls coupled to a silicon waveguide," *IEEE Photon. J.*, vol. 7, no. 2, Apr. 2015, Art. no. 6100209.

[28] Y. Lin et al., "Characterization of hybrid InP-TriPleX photonic integrated tunable lasers based on silicon nitride (Si_3N_4/SiO_2) microring resonators for optical coherent system," *IEEE Photon. J.*, vol. 10, no. 3, pp. Jun. 2018, Art. no. 1400108.

[29] J. Zhang et al., "III-V-on-Si DFB laser with co-integrated power amplifier realized using micro-transfer printing," *IEEE Photon. Technol. Lett.*, vol. 35, no. 11, pp. 593–596, Jun. 2023.

[30] E. Soltanian et al., "Micro-transfer-printed narrow-linewidth III-V-on-Si double laser structure with a combined 110 nm tuning range," *Opt. Exp.*, vol. 30, no. 22, pp. 39329–39339, 2022.

[31] B. Haq et al., "Micro-transfer-printed III-V-on-silicon C-band distributed feedback lasers," *Opt. Exp.*, vol. 28, no. 22, pp. 32793–32801, 2020.

[32] Y. Liu et al., "Micro-transfer printing of O-band InAs/GaAs quantum-dot SOAs on silicon photonic integrated circuits," *Photon. Res.*, vol. 13, no. 5, pp. 1341–1352, 2025.

[33] X. Sun, H.-C. Liu, and A. Yariv, "Adiabaticity criterion and the shortest adiabatic mode transformer in a coupled-waveguide system," *Opt. Lett.*, vol. 34, no. 3, pp. 280–282, 2009.

[34] S. Birner et al., "Nextnano: General purpose 3-D simulations," *IEEE Trans. Electron Devices*, vol. 54, no. 9, pp. 2137–2142, Sep. 2007.

[35] L. A. Coldren, S. W. Corzine, and M. L. Mashanovitch, *Diode Lasers and Photonic Integrated Circuits*. Hoboken, NJ, USA: Wiley, 2012.

[36] R. Nagarajan, M. Ishikawa, T. Fukushima, R. S. Geels, and J. E. Bowers, "High speed quantum-well lasers and carrier transport effects," *IEEE J. Quantum Electron.*, vol. 28, no. 10, pp. 1990–2008, Oct. 1992.

[37] B. R. Bennett, R. A. Soref, and J. A. Del Alamo, "Carrier-induced change in refractive index of InP, GaAs and InGaAsP," *IEEE J. Quantum Electron.*, vol. 26, no. 1, pp. 113–122, Jan. 1990.

[38] P. Blood, S. Colak, and A. I. Kucharska, "Influence of broadening and high-injection effects on GaAs-AlGaAs quantum well lasers," *IEEE J. Quantum Electron.*, vol. 24, no. 8, pp. 1593–1604, Aug. 1988.